nature communications

Article

https://doi.org/10.1038/s41467-024-52784-7

Robust flat bands in twisted trilayer graphene moiré quasicrystals

Received: 2 February 2024

Accepted: 12 September 2024

Published online: 30 September 2024

Check for updates

Chen-Yue Hao[1,2,8], Zhen Zhan[3,8] ✉, Pierre A. Pantaleón[3], Jia-Qi He[1,2], Ya-Xin Zhao[1,2], Kenji Watanabe[4], Takashi Taniguchi[5], Francisco Guinea[3,6,7] & Lin He[1,2] ✉

Moiré structures formed by twisting three layers of graphene with two independent twist angles present an ideal platform for studying correlated quantum phenomena, as an infinite set of angle pairs is predicted to exhibit flat bands. Moreover, the two mutually incommensurate moiré patterns among the twisted trilayer graphene (TTG) can form highly tunable moiré quasicrystals. This enables us to extend correlated physics in periodic moiré crystals to quasiperiodic systems. However, direct local characterization of the structure of the moiré quasicrystals and of the resulting flat bands are still lacking, which is crucial to fundamental understanding and control of the correlated moiré physics. Here, we demonstrate the existence of flat bands in a series of TTGs with various twist angle pairs and show that the TTGs with different magic angle pairs are strikingly dissimilar in their atomic and electronic structures. The lattice relaxation and the interference between moiré patterns are highly dependent on the twist angles. Our direct spatial mappings, supported by theoretical calculations, reveal that the localization of the flat bands exhibits distinct symmetries in different regions of the moiré quasicrystals.

Two-dimensional (2D) moiré superlattices are ideal platforms to explore strongly correlated phases due to the presence of nearly flat bands, where the Coulomb interactions dominate over the kinetic energy[1–3]. This can be achieved by controlling the twist angle and was first observed in twisted bilayer graphene (TBG) with a special twist angle ~1.1° (the so-called magic angle)[4–9]. The observed correlated insulator states, superconductivity, quantum anomalous Hall effect and ferromagnetic Chern insulators in the magic-angle TBG have sparked substantial research on various 2D moiré systems[10–23], such as twisted trilayer graphene (TTG)[10–14], twisted double-bilayer graphene[15,16], and twisted transition metal dichalcogenides (TMDC)[19–23], aiming at a deeper understanding of the underlying moiré physics.

Recently, particular attentions have been focused on the TTG[10–14,24–31], which is predicted to exhibit robust flat bands in an infinite set of magic-angle pairs[30,32–35]. Such a flexible system provides a more versatile platform for exploring the flat bands-related novel correlated phases. The TTG is characterized by two independent twist angles, θ_{TM} and θ_{MB}, which correspond to the rotation angles of top (T) to middle (M) layers, and M to bottom (B) layers, respectively. In the case where the ratio θ_{TM}/θ_{MB} is away from plus or minus one, two moiré lattices with different periodicities generate a class of incommensurate structures, named moiré quasicrystals[25]. The quasiperiodicity is defined on moiré length and is formed due to the incommensurability between the two moiré lattices. We emphasize that the moiré quasicrystals do not exhibit the rotational symmetries of the usual type of quasicrystal[36–38]. Very recently[25], superconductivity was observed in a TTG moiré quasicrystal with an angle pair ($\theta_{TM} = 1.41°$, $\theta_{MB} = -1.88°$), suggesting that the strict periodic

[1]Center for Advanced Quantum Studies, School of Physics and Astronomy, Beijing Normal University, Beijing 100875, China. [2]Key Laboratory of Multiscale Spin Physics, Ministry of Education, Beijing 100875, China. [3]IMDEA Nanoscience, Faraday 9, 28049 Madrid, Spain. [4]Research Center for Functional Materials, National Institute for Materials Science, Tsukuba, Japan. [5]International Center for Materials Nanoarchitectonics, National Institute for Materials Science, Tsukuba, Japan. [6]Donostia International Physics Center, Paseo Manuel de Lardizábal 4, 20018 San Sebastián, Spain. [7]Ikerbasque, Basque Foundation for Science, 48009 Bilbao, Spain. [8]These authors contributed equally: Chen-Yue Hao, Zhen Zhan. ✉e-mail: zhenzhanh@gmail.com; helin@bnu.edu.cn

structure is not a prerequisite for correlated physics. Therefore, the TTG is a convenient family for the study of novel correlated phenomena in moiré quasiperiodic systems. However, up to now, only few experiments on quasicrystals based on 2D materials have been investigated, for example, scanning tunneling microscopy (STM) and nano angle-resolved photoemission spectra (ARPES) measurement on dodecagonal 30° twisted bilayer WSe_2[36], ARPES measurement on dodecagonal 30° TBG[37,38], transport measurement[25] and STM[26,30] on TTG moiré quasicrystals. In this work, we present local characterization of a series of the TTG moiré quasicrystals ($\theta_{TM}/\theta_{MB} \neq -1$) via STM and scanning tunneling spectroscopy (STS). We observe spectroscopic signatures of the flat bands in a collection of TTGs, which provide direct confirmation of the theoretically predicted magic phase in such moiré quasicrystals. The spatial distributions of the flat bands in different regions of the TTGs are directly imaged in the STM measurements, showing distinct crystal symmetries. Our experiments supported by theoretical calculations show that the moiré pattern reconstruction and interference in the TTGs strongly depend on the twist angles.

Results

The structural properties

A schematic of our experimental set-up in the STM measurement is shown in Fig. 1a. The TTG samples with controlled twist angles (θ_{TM}, θ_{MB}) were fabricated by a dry-transfer technique on a hexagonal-boron nitride (hBN) substrate (Methods). The graphene layers are intentionally misaligned with the hBN to alleviate substrate effects. In our discussion, we assume that the two angles in the TTG are approximately commensurate, $\theta_{TM} \approx m\theta_0, \theta_{MB} \approx n\theta_0$, where m and n are coprime integers. Here θ_0 is approximated to give a period $l_{\theta_0} \approx a/[2\sin(\frac{\theta_0}{2})]$ if we neglect the angle between the two Brillouin zones defined by θ_{TM} and θ_{MB}, being a the lattice constant of graphene, as reported in refs. 30,32. It has been demonstrated theoretically that the flat bands appear in many different angle ratio (θ_{TM}/θ_{MB}) with an

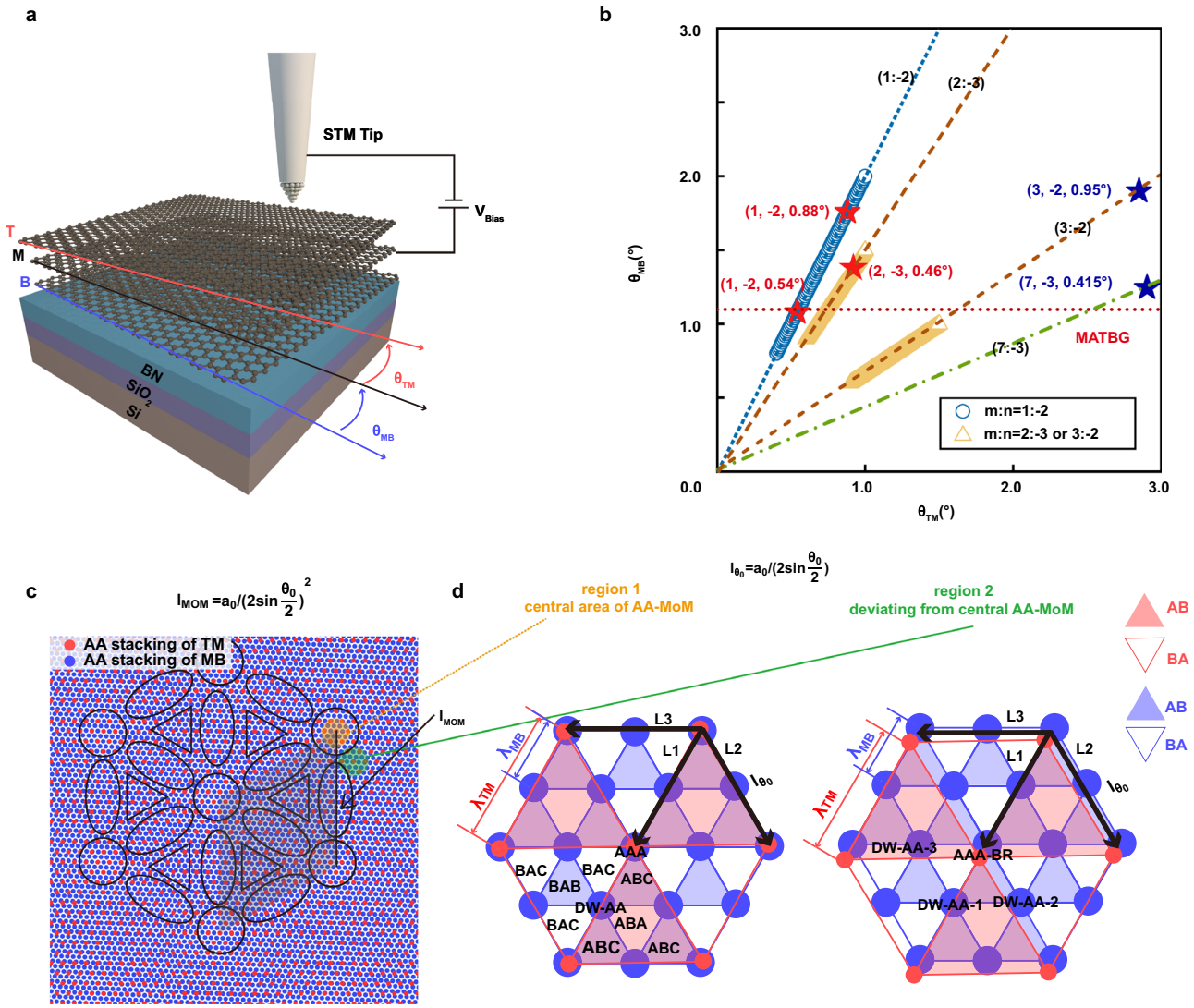

Fig. 1 | Schematic illustration of the MoM and calculated magic-angle pairs (θ_{TM}, θ_{MB}) in TTG. a Schematic of the STM set-up of the TTG device. **b** Calculated magic-angle pairs (θ_{TM}, θ_{MB}) for TTG with {1, −2}, {2, −3}, and {3, −2}. The magic-angle pairs (sample 3–5) measured in our experiment are marked by red stars and annotated by (m, n, θ_0). Sample 1 and 2 (see Supplementary Fig. 12 for detailed information) are marked by the blue stars. **c** Schematic of the MoM pattern in TTG with {1, −2}. The black quadrangle represents the unit cell of the MoM pattern. The circles represent the AA-MoM, the triangles represent the AB/BA-MoM, and the ovals represent the DW-MoM. **d** Local structures of the l_{θ_0} pattern in the central area of AA-MoM (region 1) and area deviating from AA-MoM (region 2) of the TTG. The filled circles, filled triangles, and empty triangles indicate AA, AB, and BA stacking of individual moiré patterns, respectively. The stacking configurations of DW-AA along the three directions are the same in region 1, but they are different in region 2, which are labeled as DW-AA-1, DW-AA-2 and DW-AA−3, respectively. Therefore, the C_{3z} rotation symmetry is preserved in region 1 but broken in region 2.

Table 1 | The detailed information about the five samples in our experiment

Category		m	θ_{TM} (°)	λ_{TM} (°)	n	θ_{MB} (°)	λ_{MB} (nm)	θ_O (°)	l_{θ_o} (nm)	l_{MoM}(nm)
Case 1	Sample 1	3	2.85	4.95	−2	−1.9	7.42	0.95	14.84	894.9
	Sample 2	7	2.91	4.85	−3	−1.25	11.32	0.415	33.98	4689.1
Case 2	Sample 3	1	0.54	26.11	−2	−1.08	13.05	0.54	26.11	2769.5
	Sample 4	1	0.88	16.02	−2	−1.76	8.01	0.88	16.02	1042.9
	Sample 5	2	0.92	15.32	−3	−1.38	10.21	0.46	30.64	3816.6

For each sample, we assume that the two angles, θ_{TM} and θ_{MB} are approximately commensurate, $\theta_{TM} \approx m\theta_O, \theta_{MB} \approx n\theta_O$, where m and n are coprime integers. Here, θ_{TM}, θ_{MB} and θ_O are approximated to give four periods $\lambda_{TM} \approx a/[2\sin(\frac{\theta_{TM}}{2})]$, $\lambda_{MB} \approx a/[2\sin(\frac{\theta_{MB}}{2})]$, $l_{\theta_o} \approx a/[2\sin(\frac{\theta_O}{2})]$ and $l_{MoM} = a/[2\sin(\frac{\theta_O}{2})]^2$.

infinite set of θ_O, i.e., a magic phase[30,32]. For example, the continuum calculations of angle pairs (θ_{TM}, θ_{MB}) with $\{m = 1, n = -2\}$ and $\{m = 2, n = -3\}$ predict an infinite collection of magic θ_O that possess flat bands (Fig. 1b). In the limit of $|\theta_{TM}| \ll |\theta_{MB}|$ or $|\theta_{TM}| \gg |\theta_{MB}|$, TTG decomposes into a TBG and monolayer graphene that acts as a weak perturbation in the low-energy bands. Therefore, the magic-angle curve in Fig. 1b approaches the TBG magic angle. For the formation of the flat bands in the magic-angle phase, we identify two distinct cases: TTG with a relatively strong strength of the moiré coupling between two moiré patterns resulting in hybridized flat bands, and a (slightly) decoupled TTG that can be decomposed into a magic-angle TBG plus a weak perturbation from a monolayer graphene[32,39–41]. A direct experimental confirmation of the predicted magic-angle phase is highly demanded. Furthermore, theoretical investigations have shown that lattice relaxation plays a crucial role in the TTG[29,31]. In the case of $\theta_{TM}/\theta_{MB} \approx \pm 1$, the θ_O is tiny with $\theta_O \ll \theta_{TM}, \theta_{MB}$. Subsequently, structure reconstruction leads to the formation of a single-moiré structure over a large area with a length l_{θ_o}[30]. In this work, our focus is on the quasicrystal cases where the ratio θ_{TM}/θ_{MB} is away from one, for instance, $\frac{\theta_{TM}}{\theta_{MB}} \approx -\frac{1}{2}, -\frac{1}{3}, -\frac{2}{3}, -\frac{3}{4}\ldots$. In this context, both θ_{TM} and θ_{MB} not only give rise to moiré periods λ_{TM} and λ_{MB} respectively, and quasiperiodicity l_{θ_o}, but also results in a super-long-range moiré-of-moiré (MoM) periodicity[32] with length $l_{MoM} = a/[2\sin(\frac{\theta_O}{2})]^2$. The MoM consists of three distinct types of high-symmetry stacking configurations: AA-MoM, BA/AB-MoM, DW-MoM, as schematically shown in Fig. 1c for the case $\frac{\theta_{TM}}{\theta_{MB}} \approx -\frac{1}{2}$. The incommensurability of the two periodicities λ_{TM} and λ_{MB} produces moiré-scale quasiperiodicity[25] with length of l_{θ_o}, as schematically shown in Fig. 1d. A distinctive feature of the MoM is that the C_{3z} symmetry of stacking orders is preserved in the AA-MoM and BA/AB-MoM regions, while it is broken in a general stacking region, for instance, the region 2 that is deviated from the AA-MoM region 1 (Fig. 1d). Especially, in Fig. 1d, the region 1 consists of AAA, ABC, BAB and BAC high-symmetry stackings, whereas the region 2 composes of AAA-BR, DW-AA-1, DW-AA−2 and DW-AA-3 stackings, being AAA-BR, a stacking deviated from the AAA stacking with a lateral shift. However, a direct local characterization of the MoM and lattice reconstruction in TTG quasicrystals has so far been lacking.

In this work, five TTG samples with different twist angle pairs (θ_{TM}, θ_{MB}) are studied. The detailed structural information of the five TTG samples is listed in Table 1. According to the values of θ_{TM} and θ_{MB}, we divided the TTG into two cases. The first case is that at least one of the twisted angles θ_{TM} and θ_{MB} is relatively large (samples 1 and 2). Meanwhile, the coupling strength between the two moiré lattices $\lambda_{\theta_{TM}}$ and $\lambda_{\theta_{MB}}$ is relatively weak. The second case (samples 3, 4, and 5) is the magic-angle region of which the coupling strength is relatively strong. The positions of the five samples are shown with stars of different colors (blue and red for the cases 1 and 2, respectively) in Fig. 1b. Figure 2a shows a representative STM image of a TTG with the twist angle pair (2.85°, −1.9°), i.e., the sample 1 with $\theta_O = 0.95°$, $m = 3$, and $n = -2$. The moiré superlattices with $\lambda_{TM} = 4.95$ nm, $\lambda_{MB} = 7.42$ nm, and the supermodulation $l_{\theta_o} = 14.84$ nm can be clearly identified in both the STM image and its fast Fourier transform (FFT) image (Fig. 2b). The unit cell of the MoM is estimated as $l_{MoM} = a/[2\sin(\frac{\theta_O}{2})]^2 \approx 895$ nm, which is too large to be directly imaged in the STM measurements. However, we can identify the AA-MoM region of the MoM according to the local C_{3z} symmetry of the moiré structures, as summarized in Fig. 2c–f. Figure 2c, e shows two representative STM images recorded in the central area of the AA-MoM region and ~100 nm away from the AA-MoM region, respectively. Although the moiré superlattices λ_{TM}, λ_{MB}, and l_{θ_o} are identical in the two STM images, they exhibit quite different local symmetry of the moiré patterns: the C_{3z} symmetry is preserved in Fig. 2c, whereas it is broken in Fig. 2e. Such a result is verified in the topography profiles along L_1, L_2 and L_3, as shown in Fig. 2d, f. In the central area of the AA-MoM region, the three profiles exhibit the same period $\lambda_{TM} = 4.95$ nm with a supermodulation $l_{\theta_o} = 14.84$ nm (Fig. 2d). However, in the area away from the AA-MoM region, the profile lines L_1, L_2 and L_3 exhibit noticeably different features in both periodicity and magnitude, as shown in Fig. 2f.

The electronic properties

In our experiment, the same STM measurements are carried out in all the studied TTG quasicrystals and similar features are observed in the local moiré symmetry of the MoM. Figures 3 and 4 show representative results obtained in two TTG samples, i.e., the sample 3 with a twist angle pair (0.54°, −1.08°) and $\theta_O = 0.54°$, and the sample 4 with a twist angle pair (0.88°, −1.76°) and $\theta_O = 0.88°$. All the information also can be clearly identified in both the STM image (Figs. 3a and 4a) and its FFT images (Figs. 3b and 4b). First, we can identify the studied regions of the MoM according to both the local moiré symmetry in the STM images, as shown in Figs. 3a and 4a, and the high-symmetry profile lines in Figs. 3c and 4c (local strain slightly affects the moiré periods in the three directions, but has a small effect on the atomic structures of different stacking regions). Our measurement further indicates that the different stacking configurations of the MoM not only affect the moiré patterns in the STM images, but also strongly influence the spatial distributions of the flat bands in the TTG. The left panels of Figs. 3d and 4d show typical dI/dV spectra recorded in the AAA and AAA-BR regions of samples 3 and 4, respectively. The low-energy pronounced peaks in the spectra are attributed to the high density of states (DOS) of the flat bands in the TTG. Our theoretical (TB) calculations, considering the twist angle pairs determined in our experiment, confirm the existence of flat bands, which result in high local DOS near the Fermi level (Figs. 3e and 4e). The right panels of Figs. 3d and 4d display the measured energy-fixed STS, i.e., dI/dV, maps over several moiré unit cells, which directly reflect the spatial distributions of the flat bands. In the central area of the AA-MoM region, similar to the TBG, the flat bands are concentrated on the AAA stacking regions, confirming the preservation of the C_{3z} symmetry. However, in the area away from the center of the AA-MoM region, the flat bands are distributed in the AAA-BR and DW-AA-2 stacking regions. Moreover, the dI/dV spectra measured in the DW-AA-1, DW-AA-2 and DW-AA−3 are different (see Supplementary Note 6). Thus, in this region, the C_{3z} symmetry is broken. In fact, from the structure in Fig. 1d, the region 2

https://doi.org/10.1038/s41467-024-52784-7

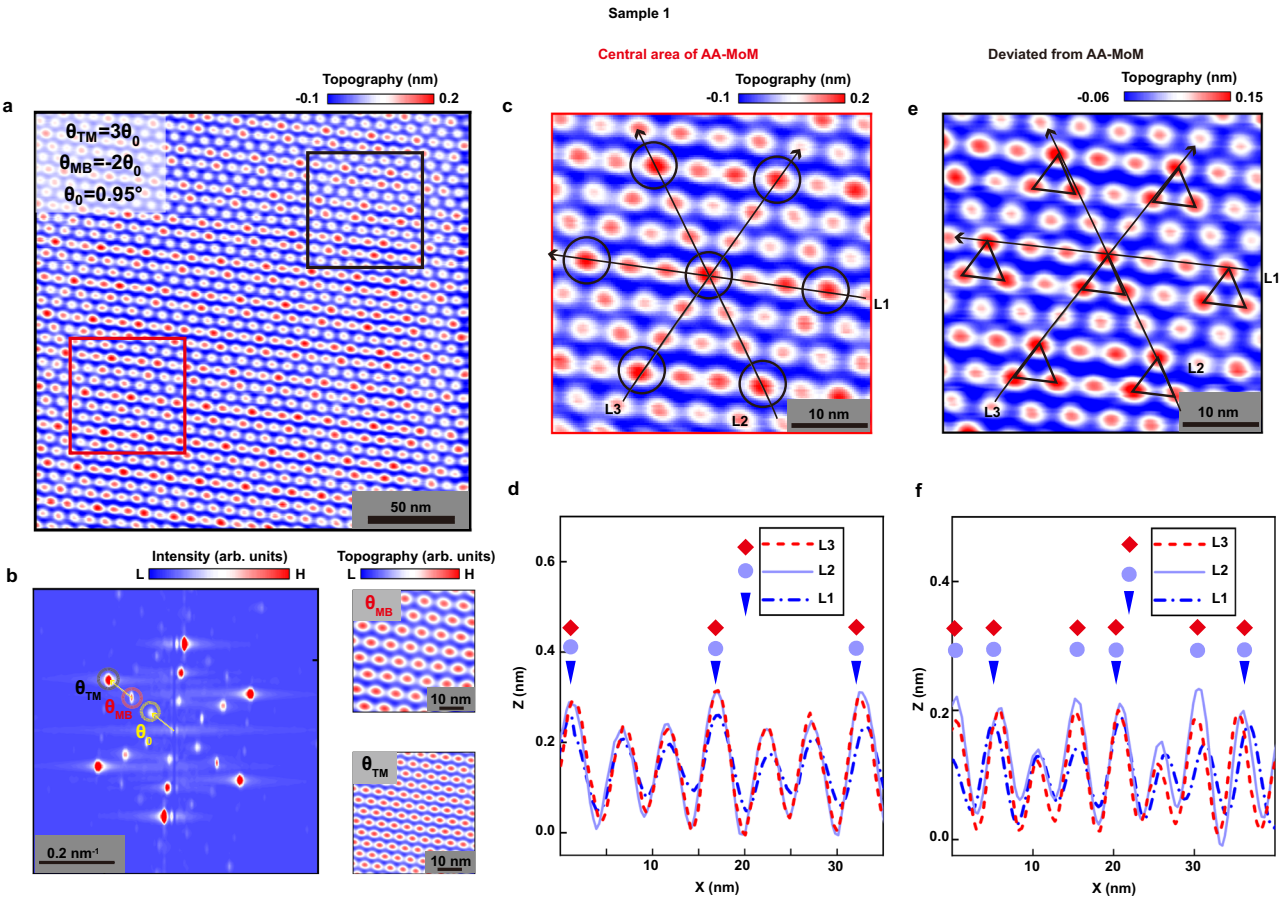

Fig. 2 | Local characterization of stacking configurations in a TTG. a STM topography of sample 1 (V_{bias} = 0.6 V, I = 100 pA). **b** Left panel: FFT image of **a**. The circles mark the reciprocal moiré lattices of θ_{TM} (black), θ_{MB} (red) and θ_0 (yellow). Right panel: Fourier-filtered images based on the first-order moiré spots of θ_{MB} and θ_{TM} in the left panel. **c**, **e** Zoom-in images of red and black frames in **a**, representing the central area of AA-MoM and the region deviating from AA-MoM, respectively. The circles represent the AAA stacking, while the triangles represent the AAA-BR stacking. The C_{3z} rotation symmetry in **c** is preserved while it is broken in **e**. **d**, **f** Height profile of the lines along the three different directions in **c** and **e**, respectively. Inverted triangles, circles and quadrilaterals in different colors refer to the AAA or AAA-BR stackings along the three different directions. The different arrangements of stackings along the three directions also reveal the breaking of the C_{3z} rotation symmetry.

deviated from the AA-MoM center only has $C_{2x}T$ symmetry. In Figs. 3e and 4e, we project the theoretical DOS of the flat bands onto the top graphene layer, where the electronic states are mainly detected in the STM measurements. The distribution in Fig. 4d is slightly different to that in Fig. 4e, but it is very similar to local DOS on the middle layer (see Supplementary Fig. 16b). It implies that the experimental feature has some contributions from the middle layer. Our theoretical results effectively capture the key features observed in our experiment.

Our STS measurements indicate that all the studied TTG samples in this work exhibit pronounced low-energy peaks in the spectra (see Figs. 3 and 4 and Supplementary Fig. 13). Interestingly, the width of these low-energy DOS peaks depends sensitively on the twist angle pairs (see Supplementary Note 8). We use the full width at half maximum (FWHM) of the DOS to represent the width, and all the FWHM are obtained from a multi-Gaussian fitting procedure. To further understand our experimental results, we calculated the bandwidth of the low-energy electronic states from the band structure of the TTG systems with different angle pairs via a continuum model (see Supplementary Fig. 8). Figure 5b, c shows the continuum results of the TTG with (θ_{TM}, θ_{MB}) for $\{m = 1, n = -2\}$ and $\{m = 3, n = -2\}$, where is clear that the bandwidths strongly depend on the values of m, n and θ. Our experiment, supported by theoretical calculations, indicates that TTG can exhibit robust flat bands at an infinite set of magic-angle pairs. The observed bandwidths are larger than that obtained in the calculations, which is presumably due to thermal broadening of temperature, strain[42], reconstruction[43–45], and electron-electron interactions arising from the partial filling of the flat bands[46]. Moreover, there are several degrees of freedom to tune the bandwidth, a crucial aspect for realizing novel correlated phases.

Another significant finding related to the flat bands is their distinct layer distributions in the TTG, depending on the twist angle pair. Figure 5a shows representative STS spectra recorded in sample 1 with the twisted angle pair (2.85°, -1.9°). The two peaks flanking the Fermi level in the representative spectra are noticeably weaker compared to the calculated results. Meanwhile, the left top panel of Fig. 5d shows the STS map of the DOS peak at 40 mV in sample 1, which follows the twist angle of θ_0 but with a very weak signal. To understand the reason for this observed weak signal, we simulated the distribution of this LDOS peak on each layer. As shown in the other panels in Fig. 5d, the LDOS is mainly concentrated on the middle and bottom layers, while the other two strong LDOS peaks are primarily concentrated on the top and middle layers (see Supplementary Fig. 16d–f). This result implies that the electronic properties of sample 1 can be understood as a superposition of two TBG (Supplementary Note 3). To gain a comprehensive understanding of this, we calculated the DOS of sample 1 and the DOS of two TBG with twist angles 2.85° and 1.9° respectively, as shown in Fig. 5f. For comparison, we also calculated the DOS of sample 4 and the DOS of two TBG with twisted angles 0.88° and 1.76° respectively, as

https://doi.org/10.1038/s41467-024-52784-7

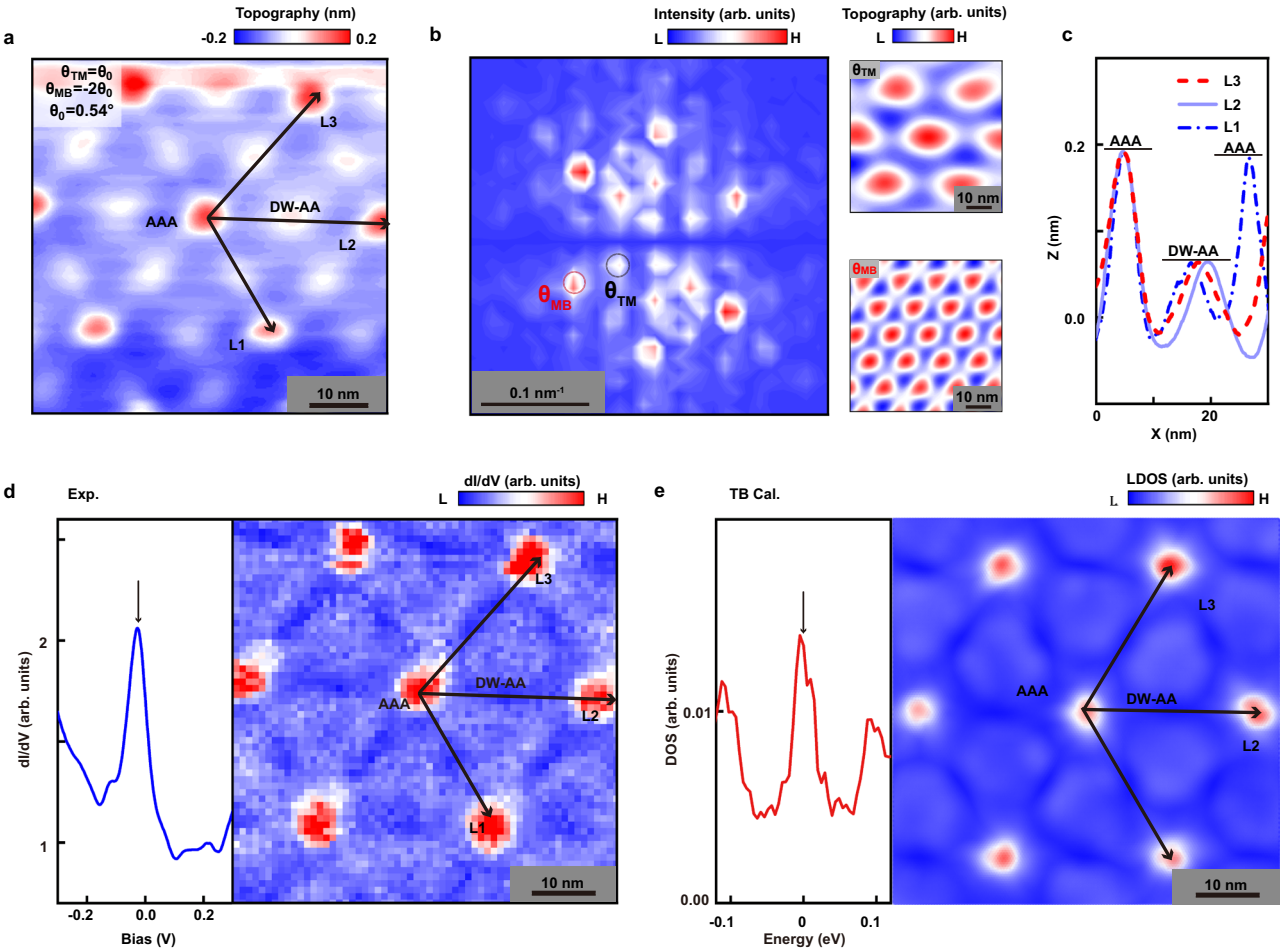

Fig. 3 | Flat bands and their spatial distribution in Sample 3. a STM topographies of sample 3 (V_{bias} = 0.4 V, I = 300 pA). **b** Left panel: the FFT image of **a**. The circles mark the reciprocal moiré lattices of θ_{TM} (black) and θ_{MB} (red). The right panel: Fourier-filtered images based on the first-order moiré spots of θ_{MB} and θ_{TM} in the left panel. **c** Height profile lines along the three different directions in **a**. The height differences between AAA and DW-AA stackings along the three directions are almost the same. **d** Left panel: dI/dV spectra recorded in AAA stacking. Right panel: dI/dV maps of the area in **a** with the fixed sample bias, −20 mV. **e** Left panels: tight-binding calculations of the DOS of the TTG with $\theta_{TM} = \theta_0$, $\theta_{MB} = -2\theta_0$ and $\theta_0 = 0.54°$. Right panels: calculated DOS on the top layer of the TTG at $E = 0$ eV.

shown in Fig. 5e. It is noticeable that the DOS of the sample 1 is nearly identical to the superposition of that of the two TBG. This implies that the electronic properties of sample 1 can be understood as a superposition of the two TBG, and the coupling between θ_{TM} and θ_{MB} is rather weak. While the experimental results show that the flat bands of sample 3 and 4 have a strong distribution in the top layer (see Figs. 3d and 4d). In fact, according to our theory calculations, the flat bands in these two systems distribute evenly in the three layers, and the coupling between θ_{TM} and θ_{MB} is relatively strong (see Supplementary Fig. 1c and Supplementary Fig. 16a–c).

The influence of structure reconstructions

In our experiment, the observed structure reconstruction is significantly different from the case of $\theta_{TM}/\theta_{MB} \approx \pm 1$. In the studied five TTG samples, the supermoiré scale ($\sim l_{MoM}$) lattice relaxation is weak and does not result in a large-area single-moiré structure, as observed in the case of $\theta_{TM}/\theta_{MB} \approx \pm 1$[29–31,47]. Instead, the observed lattice relaxations behave similarly to the TBG case[48–51]. For instance, when one of the twist angles in the angle pair is small (<~1°), the AAA regions shrink, and the ABA regions expand to a triangular domain separated by sharp domain walls (Fig. 3). Similarly, our theoretical calculation indicates that the lattice relaxation renormalizes the Fermi velocity of the narrow bands (Supplementary Figs. 1–3). The slight difference is that the lattice relaxation effect in the TTG is not only dependent on the magnitude of the twist angles, but also on the ratio θ_{TM}/θ_{MB}. Up to now, the structure reconstruction of the TTG has been investigated only in a few angle pairs, and how it behaves in other angle pairs is still unclear.

Continuum model with Hartree potential

To gain insight into the electronic structure, we complement our TB calculations with a continuum model to conduct a detailed analysis of the electronic properties of all samples (see Supplementary Note 4). Considering the various local stackings across the MoM periodicity in the continuum model, we found that although the electronic structure depends on stacking, the flat bands persist (see Supplementary Fig. 7 and Note 10)[32,41,52]. We notice that there is a slight difference between the DOS obtained with the TB calculations and the dI/dV spectra. As discussed before, this discrepancy may be related to the thermal broadening of temperature, strain[42], reconstruction[43–45], and electron-electron interactions[46]. In fact, our theoretical analysis reveals that all combinations exhibit narrow bands in the middle of the spectrum whose bandwidth is comparable with the effective long-range Coulomb interaction strength. Therefore, we can estimate the strength of electron-electron interactions and obtain the filling-dependent renormalized bands through a self-consistent Hartree potential (see Supplementary Note 4). Focusing solely on samples featuring well-defined and isolated narrow bands, we observed electronic band renormalization with filling and pinning of the Fermi energy to the van Hove

https://doi.org/10.1038/s41467-024-52784-7

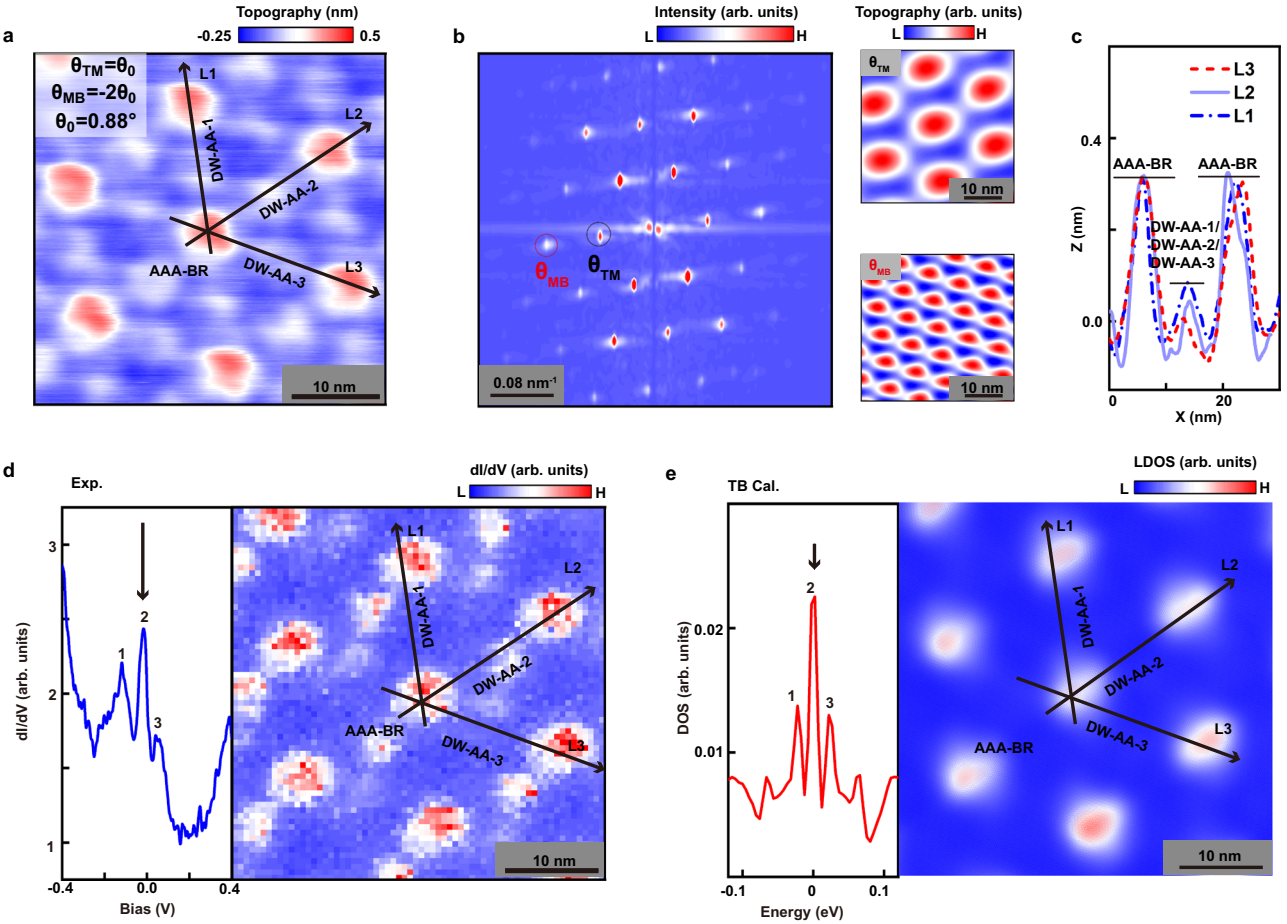

Fig. 4 | Flat bands and their spatial distribution in Sample 4. a STM topographies of sample 4 ($V_{bias} = -0.8$ V, $I = 300$ pA). **b** Left panel: The FFT image of **a**. The circles mark the reciprocal moiré lattices of θ_{TM} (black) and θ_{MB} (red). The right panel: Fourier-filtered images based on the first-order moiré spots of θ_{MB} and θ_{TM} in the left panel. **c** Height profile lines along the three different directions in **a**. The height differences between AAA-BR and DW-AA along three directions are quite different because of the different stacking configurations, labelled as DW-AA-1, DW-AA-2, and DW-AA−3. **d** Left panel: dI/dV spectra recorded in AAA-BR stacking. Right panel: dI/dV maps of area in **a** with the fixed sample bias, −50 mV. **e** Left panels: Tight-binding calculations of the DOS of the TTG with $\theta_{TM} = \theta_0$, $\theta_{MB} = -2\theta_0$ and $\theta_0 = 0.88°$. Right panels: Calculated DOS on the top layer of the TTG at $E = 0$ eV.

singularity, closely resembling the effects observed in TBG. Our findings indicate that, contrary to helical TTG where the interaction-induced band renormalization is weak[53], in our samples the electrostatic effects appear to be significant. On the other hand, we also found that, to properly describe the electrostatic interactions in our systems, we require a Hartree potential whose Fourier expansion is beyond a first harmonic approximation (see Supplementary Note 5). The additional Fourier components indicate a quasicrystal structure, which is also reflected in the real-space shape of the Hartree potential (see Supplementary Note 5). Therefore, the presence of a strong Hartree potential and its dependence on doping suggests that electrostatic interactions play a significant role in these systems.

Discussion

In summary, the structural and electronic characteristics of the TTG are carefully studied via STM and STS measurements, complemented with a direct comparison with theory. We demonstrate the existence of robust flat bands in TTG with different twist angle pairs, identifying the theoretically predicted magic phases. Specifically, the flat bands in this system are determined by the quasiperiodicity, in the scale of several nanometers, arising from incommensurability between two moiré lattices. Our experiment indicates that TTG is a powerful platform to explore the strongly correlated physics embedded in the flat bands of quasicrystals.

Methods

Device fabrication

The device was fabricated by using the "tear and stack" method[54]. A thick hBN was picked up by Polydimethylsiloxane (PDMS) film while the graphene exfoliated on SiO2/Si chips was pre-cut into three parts by atomic force microscopy tip. Next, the three parts were picked by the thick hBN piece by piece with manually adjusted twisted angles. Finally, with the help of another PDMS, the whole heterostructure was upturned and transferred to the SiO_2/Si chip with a pre-coated Au/Cr electrode and the graphite flake was used to connect the electrode with the sample. In order to clean the device surface, we annealed the samples at 200 °C for about 8 hours in LPCVD and ultrahigh vacuum before the STM measurements. Note that in this work we fabricated and measured five separated samples.

STM measurements

STM/STS measurements were performed in low-temperature (78 K) and ultrahigh-vacuum (~10^{-10} Torr) scanning probe microscopes [USM-1400] from UNISOKU. The tips were obtained by chemical etching from a tungsten wire. The differential conductance (dI/dV) measurements were taken by a standard lock-in technique with an ac bias modulation of 5 mV and 793 Hz signal added to the tunnelling bias, and all the STM measurements were performed in a constant-current mode. The STM tip was obtained by etching tungsten wire and

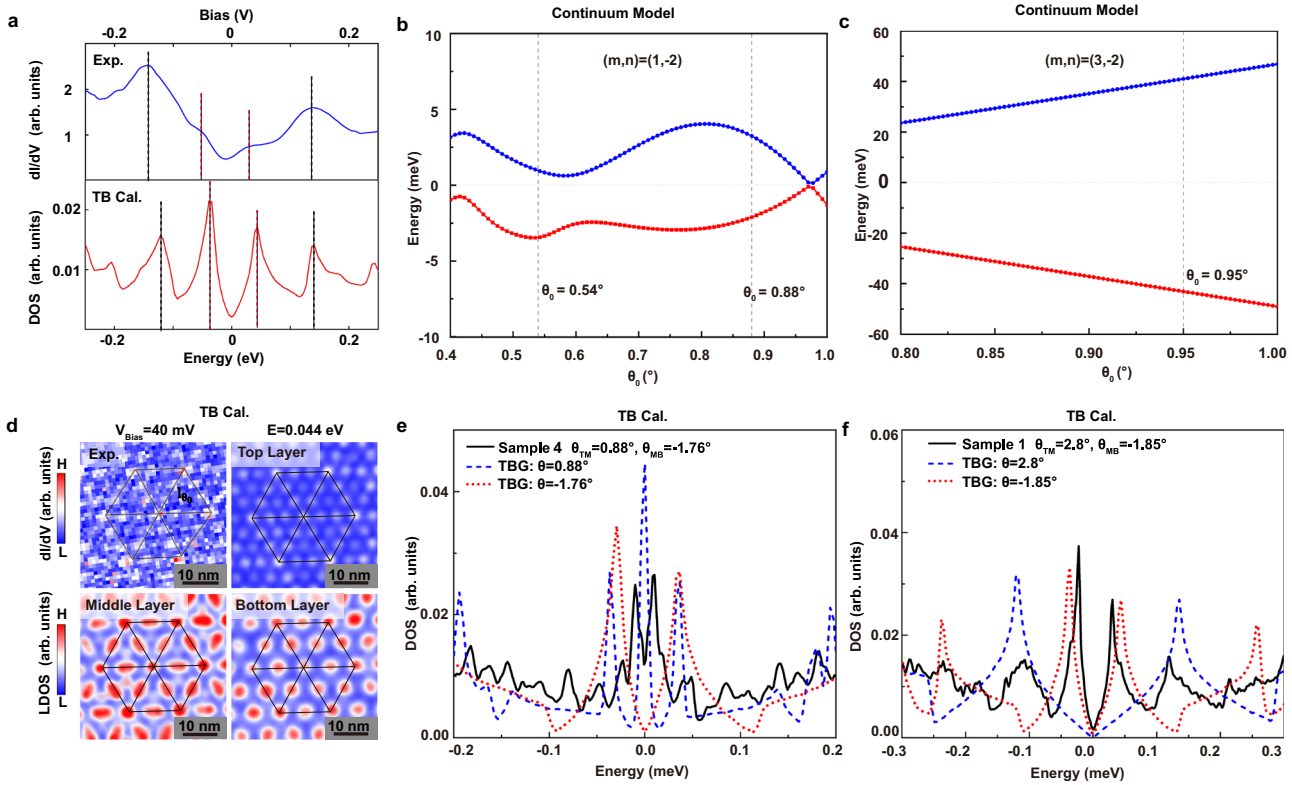

Fig. 5 | Electronic properties of TTGs with various twist angle pairs. a Upper panel: dI/dV spectra recorded in the AAA-BR stacking region (illustrated in the Fig. 1d) of the sample 1. Lower panel: tight-binding calculations of the DOS of a TTG with ($\theta_{TM} = 3\theta_0$, $\theta_{MB} = -2\theta_0$ and $\theta_0 = 0.95°$). **b**, **c** Energy average of K points of the band edges (valence band (red), conduction band (blue)) in the BZ for different θ_0 with angle pairs $(m, n) = (1, -2)$ and $(3, -2)$. The dotted lines represent the positions of sample 3, 4, and 1, respectively. The samples 3 ($\theta_0 = 0.54°$) and 4 ($\theta_0 = 0.88°$) have narrow bands near the charge neutrality point (CNP), while the width of the band near the CNP is beyond 40 mV for sample 1 ($\theta_0 = 0.95°$). **d** Upper left panel: dI/dV maps from area deviated from the central region of AA-MoM in sample 1 with the fixed sample bias, 40 mV. Other panels: calculated DOS on the top, middle, bottom layers of sample 1 at $E = 0.044$ eV. **e** The calculated DOS of sample 4 (black solid line) and TBG with $\theta = 0.88°$ (blue dashed line) and $\theta = -1.76°$ (red dotted line). **f** The calculated DOS of sample 1 (black solid line), and of the TBG with $\theta = 2.8°$ (blue dashed line) and $\theta = -1.85°$ (red dotted line). For simplicity, we compare the DOS of the moiré structures without lattice relaxations. The number and location of peaks in sample 1 are same to the combination of the two TBG, which indicates the weak coupling strength of the two moiré patterns. The number and location of peaks in sample 4 are totally different to the combination of the two TBG, which means the strong coupling strength of the two moiré patterns.

calibrated to be atomically sharp in the Au surface before the measurements.

The density of states and charge distribution calculations

We employed an atomic tight-binding (TB) model to compute the density of states and LDOS map of the TTG (detailed in Supplementary Note 1–2). We used a round disk method to construct the TTG with commensurate or incommensurate twist angles[55]. Then, the samples were relaxed with the semi-classical molecular dynamics implemented in LAMMPS[56–58]. The radius of the disk was $700a$, which contained 10 million carbon atoms. To obtain the DOS and LDOS map of these complex samples, we utilized the tight-binding propagation method (TBPM) without a diagonalization process, which is implemented in the TBPLaS package[59]. Note that the TBPM method is an efficient method to deal with the system without periodicity, for example, the dodecagonal bilayer graphene quasicrystal[55].

Continuum model and Hartree calculations

We determine the electronic band structure of all samples employing a low-energy continuum model. The methodology outlined in ref. 32. is followed, considering an approximately commensurate trilayer system (detailed in Supplementary Note 4). A self-consistent Hartree calculation of the electronic bands is carried out[60] specifically for samples 3 and 4, because they are characterized by well-isolated narrow bands (detailed in Supplementary Note 4).

Data availability

The raw data generated in this study are available at https://doi.org/10.6084/m9.figshare.26787553.

Code availability

The codes that support this study are available from the corresponding author upon request.

References

1. Balents, L., Dean, C. R., Efetov, D. K. & Young, A. F. Superconductivity and strong correlations in moiré flat bands. *Nat. Phys.* **16**, 725–733 (2020).
2. Andrei, E. Y. & MacDonald, A. H. Graphene bilayers with a twist. *Nat. Mater.* **19**, 1265–1275 (2020).
3. Ren, Y.-N., Zhang, Y., Liu, Y.-W. & He, L. Twistronics in graphene-based van der Waals structures. *Chin. Phys. B* **29**, 117303 (2020).
4. Bistritzer, R. & MacDonald, A. H. Moiré bands in twisted double-layer graphene. *Proc. Natl. Acad. Sci.* **108**, 12233–12237 (2011).
5. Yin, L.-J., Qiao, J.-B., Zuo, W.-J., Li, W.-T. & He, L. Experimental evidence for non-Abelian gauge potentials in twisted graphene bilayers. *Phys. Rev. B* **92**, 081406 (2015).
6. Cao, Y. et al. Correlated insulator behaviour at half-filling in magic-angle graphene superlattices. *Nature* **556**, 80–84 (2018).
7. Cao, Y. et al. Unconventional superconductivity in magic-angle graphene superlattices. *Nature* **556**, 43–50 (2018).

8. Lopes dos Santos, J. M. B., Peres, N. M. R. & Castro Neto, A. H. Graphene bilayer with a twist: electronic structure. *Phys. Rev. Lett.* **99**, 256802 (2007).
9. Serlin, M. et al. Intrinsic quantized anomalous Hall effect in a moiré heterostructure. *Science* **367**, 900–903 (2020).
10. Hao, Z. et al. Electric field–tunable superconductivity in alternating-twist magic-angle trilayer graphene. *Science* **371**, 1133–1138 (2021).
11. Park, J. M., Cao, Y., Watanabe, K., Taniguchi, T. & Jarillo-Herrero, P. Tunable strongly coupled superconductivity in magic-angle twisted trilayer graphene. *Nature* **590**, 249–255 (2021).
12. Xu, S. et al. Tunable van Hove singularities and correlated states in twisted monolayer–bilayer graphene. *Nat. Phys.* **17**, 619–626 (2021).
13. Chen, S. et al. Electrically tunable correlated and topological states in twisted monolayer–bilayer graphene. *Nat. Phys.* **17**, 374–380 (2021).
14. Polshyn, H. et al. Electrical switching of magnetic order in an orbital Chern insulator. *Nature* **588**, 66–70 (2020).
15. Cao, Y. et al. Tunable correlated states and spin-polarized phases in twisted bilayer–bilayer graphene. *Nature* **583**, 215–220 (2020).
16. Liu, X. et al. Tunable spin-polarized correlated states in twisted double bilayer graphene. *Nature* **583**, 221–225 (2020).
17. Zheng, Z. et al. Unconventional ferroelectricity in moiré heterostructures. *Nature* **588**, 71–76 (2020).
18. Chen, G. et al. Signatures of tunable superconductivity in a trilayer graphene moiré superlattice. *Nature* **572**, 215–219 (2019).
19. Li, H. et al. Imaging two-dimensional generalized Wigner crystals. *Nature* **597**, 650–654 (2021).
20. Regan, E. C. et al. Mott and generalized Wigner crystal states in WSe2/WS2 moiré superlattices. *Nature* **579**, 359–363 (2020).
21. Tang, Y. et al. Simulation of Hubbard model physics in WSe2/WS2 moiré superlattices. *Nature* **579**, 353–358 (2020).
22. Jin, C. et al. Stripe phases in WSe2/WS2 moiré superlattices. *Nat. Mater.* **20**, 940–944 (2021).
23. Zhang, Z. et al. Flat bands in twisted bilayer transition metal dichalcogenides. *Nat. Phys.* **16**, 1093–1096 (2020).
24. Cao, Y., Park, J. M., Watanabe, K., Taniguchi, T. & Jarillo-Herrero, P. Pauli-limit violation and re-entrant superconductivity in moiré graphene. *Nature* **595**, 526–531 (2021).
25. Uri, A. et al. Superconductivity and strong interactions in a tunable moiré quasicrystal. *Nature* **620**, 762–767 (2023).
26. Kim, H. et al. Evidence for unconventional superconductivity in twisted trilayer graphene. *Nature* **606**, 494–500 (2022).
27. Liu, X., Zhang, N. J., Watanabe, K., Taniguchi, T. & Li, J. I. A. Isospin order in superconducting magic-angle twisted trilayer graphene. *Nat. Phys.* **18**, 522–527 (2022).
28. Shen, C. et al. Dirac spectroscopy of strongly correlated phases in twisted trilayer graphene. *Nat. Mater.* **22**, 316–321 (2023).
29. Nakatsuji, N., Kawakami, T. & Koshino, M. Multiscale lattice relaxation in general twisted trilayer graphenes. *Phys. Rev. X* **13**, 041007 (2023).
30. Turkel, S. et al. Orderly disorder in magic-angle twisted trilayer graphene. *Science* **376**, 193–199 (2022).
31. Yang, C., May-Mann, J., Zhu, Z., Devakul, T. Multi-moiré trilayer graphene: lattice relaxation, electronic structure, and magic angles. *Phys. Rev. B* **110**, 115434 (2024).
32. Foo, D. C. W. et al. Extended magic phase in twisted graphene multilayers. *Phys. Rev. Res.* **6**, 013165 (2024).
33. Devakul, T. et al. Magic-angle helical trilayer graphene. *Sci. Adv.* **9**, eadi6063 (2023).
34. Xia, L.-Q. et al. Helical trilayer graphene: a moir\'e platform for strongly-interacting topological bands. Preprint at https://doi.org/10.48550/arXiv.2310.12204 (2023).
35. Popov, F. K. & Tarnopolsky, G. Magic angle butterfly in twisted trilayer graphene. *Phys. Rev. Res.* **5**, 043079 (2023).
36. Li, Y. et al. Tuning commensurability in twisted van der Waals bilayers. *Nature* **625**, 494–499 (2024).
37. Ahn, S. J. et al. Dirac electrons in a dodecagonal graphene quasicrystal. *Science* **361**, 782–786 (2018).
38. Yao, W. et al. Quasicrystalline 30° twisted bilayer graphene as an incommensurate superlattice with strong interlayer coupling. *Proc. Natl. Acad. Sci.* **115**, 6928–6933 (2018).
39. Zhu, Z., Carr, S., Massatt, D., Luskin, M. & Kaxiras, E. Twisted trilayer graphene: a precisely tunable platform for correlated electrons. *Phys. Rev. Lett.* **125**, 116404 (2020).
40. Meng, H., Zhan, Z. & Yuan, S. Commensurate and incommensurate double moir\'e interference in twisted trilayer graphene. *Phys. Rev. B* **107**, 035109 (2023).
41. Mao, Y., Guerci, D. & Mora, C. Supermoir\'e low-energy effective theory of twisted trilayer graphene. *Phys. Rev. B* **107**, 125423 (2023).
42. Bi, Z., Yuan, N. F. Q. & Fu, L. Designing flat bands by strain. *Phys. Rev. B* **100**, 035448 (2019).
43. Nam, N. N. T. & Koshino, M. Lattice relaxation and energy band modulation in twisted bilayer graphene. *Phys. Rev. B* **96**, 075311 (2017).
44. Yoo, H. et al. Atomic and electronic reconstruction at the van der Waals interface in twisted bilayer graphene. *Nat. Mater.* **18**, 448–453 (2019).
45. Jiang, Y. et al. Charge order and broken rotational symmetry in magic-angle twisted bilayer graphene. *Nature* **573**, 91–95 (2019).
46. Guinea, F. & Walet, N. R. Electrostatic effects, band distortions, and superconductivity in twisted graphene bilayers. *Proc. Natl. Acad. Sci. USA* **115**, 13174–13179 (2018).
47. Craig, I. M. et al. Local atomic stacking and symmetry in twisted graphene trilayers. *Nat. Mater.* **23**, 323–330 (2024)
48. Zheng, Q. et al. Tunable sample-wide electronic kagome lattice in low-angle twisted bilayer graphene. *Phys. Rev. Lett.* **129**, 076803 (2022).
49. Ren, Y.-N. et al. Real-space mapping of local subdegree lattice rotations in low-angle twisted bilayer graphene. *Nano Lett.* **23**, 1836–1842 (2023).
50. Hao, C.-Y. et al. Creating a custom-designed moir\'e magnifying glass to probe local atomic lattice rotations in twisted bilayer graphene. *Phys. Rev. B* **108**, 125429 (2023).
51. Zhou, X.-F. et al. Coexistence of reconstructed and unreconstructed structures in the structural transition regime of twisted bilayer graphene. *Phys. Rev. B* **107**, 125410 (2023).
52. Guerci, D., Mao, Y. & Mora, C. Nature of even and odd magic angles in helical twisted trilayer graphene. *Phys. Rev. B* **109**, 205411 (2024).
53. Kwan, Y. H., Ledwith, P. J., Lo, C. F. B. & Devakul, T. Strong-coupling topological states and phase transitions in helical trilayer graphene. *Phys. Rev. B* **109**, 125141 (2024).
54. Kim, K. et al. van der Waals heterostructures with high accuracy rotational alignment. *Nano Lett.* **16**, 1989–1995 (2016).
55. Yu, G., Wu, Z., Zhan, Z., Katsnelson, M. I. & Yuan, S. Dodecagonal bilayer graphene quasicrystal and its approximants. *npj Comput. Mater.* **5**, 1–10 (2019).
56. Kolmogorov, A. N. & Crespi, V. H. Registry-dependent interlayer potential for graphitic systems. *Phys. Rev. B* **71**, 235415 (2005).
57. Los, J. H., Ghiringhelli, L. M., Meijer, E. J. & Fasolino, A. Improved long-range reactive bond-order potential for carbon. I. construction. *Phys. Rev. B* **72**, 214102 (2005).
58. Plimpton, S. Fast parallel algorithms for short-range molecular dynamics. *J. Comput. Phys.* **117**, 1–19 (1995).
59. Li, Y., Zhan, Z., Kuang, X., Li, Y. & Yuan, S. TBPLaS: a tight-binding package for large-scale simulation. *Comput. Phys. Commun.* **285**, 108632 (2023).
60. Cea, T., Walet, N. R. & Guinea, F. Electronic band structure and pinning of Fermi energy to Van Hove singularities in twisted bilayer graphene: a self-consistent approach. *Phys. Rev. B* **100**, 205113 (2019).

Acknowledgements
This work was supported by the National Key R and D Program of China (Grant Nos. 2021YFA1400100 and 2021YFA1401900), the National Natural Science Foundation of China (Grant nos. 12425405, 12141401, 11974050), and "the Fundamental Research Funds for the Central Universities". Z.Z. acknowledges support funding from the European Union's Horizon 2020 research and innovation program under the Marie Skłodowska-Curie grant agreement No 101034431 P.A.P, F.G. and Z.Z. acknowledge support from NOVMOMAT, Grant PID2022-142162NB-I00 funded by MCIN/AEI/ 10.13039/501100011033, by "ERDF A way of making Europe" and from the "Severo Ochoa" Program for Centers of Excellence in R&D (CEX2020-001039-S/AEI/10.13039/501100011033). We thank the Core Facility of Wuhan University for providing the computational resources. The devices were fabricated using the transfer platform from Shanghai Onway Technology Co. Ltd.

Author contributions
C.-Y.H. fabricated the device. C.-Y.H., J.-Q.H., and Y.-X.Z. performed the measurements. C.-Y.H., Z.Z., F.G., and L.H. analyzed the data. Z.Z. and P.A.P. provided theoretical analysis, supervised by F.G. L.H. conceived and provided advice on the experiment and analysis. K.W. and T.T. provided the hBN crystals. C.-Y.H., Z.Z., P.A.P., and L.H. wrote the manuscript with input from all co-authors.

Competing interests
The authors declare no competing interests.

Additional information
Supplementary information The online version contains supplementary material available at https://doi.org/10.1038/s41467-024-52784-7.

Correspondence and requests for materials should be addressed to Zhen Zhan or Lin He.

Peer review information *Nature Communications* thanks Zhongkai Liu, and the other, anonymous, reviewer(s) for their contribution to the peer review of this work. A peer review file is available.